2015-06-08

Spectroscopic Characterization of a Radio-Frequency Argon Plasma Jet Discharge in Ambient Air

Patrick Cullen
Technological University Dublin, pj.cullen@tudublin.ie

Vladimir Milosavljevic
Technological University Dublin, vladimir.milosavljevic@tudublin.ie

Recommended Citation

Cullen, P.J. & Milosavljevic, V. (2015) *Prog. Theor. Exp. Phys.* 2015/6, 063J01 . doi:10.1093/ptep/ptv070

PTEP

Prog. Theor. Exp. Phys. **2015**, 063J01 (17 pages)
DOI: 10.1093/ptep/ptv070

Spectroscopic characterization of a radio-frequency argon plasma jet discharge in ambient air

P. J. Cullen[1,2] and V. Milosavljević[1,3,*]

[1] *BioPlasma Research Group, Dublin Institute of Technology, Sackville Place, Dublin 1, Ireland*
[2] *School of Chemical Engineering, UNSW, Sydney, NSW 2052, Australia*
[3] *Faculty of Physics, University of Belgrade, P.O.B. 368, Belgrade, Serbia*
[*] E-mail: vm@dit.ie

Received February 12, 2015; Revised April 9, 2015; Accepted April 19, 2015; Published June 8, 2015

This study includes a detailed experimental investigation of the spatial and temporal spectroscopic emission of an argon plasma jet discharge. The study is carried out in ambient air and quenching by inflowing air species is considered. The optical emission spectroscopy of neutral atomic spectral lines and molecular bands, over a range of plasma process parameters, is investigated. Wavelength-resolved argon optical emission profiles are used to monitor the electron energy distribution function and the density of argon metastable atoms. The experimental data indicates that the argon flow rate, in a confined open-air plasma discharge, limits the impact of molecular oxygen in the creation of oxygen radicals. The absolute calibrated emission spectra facilitate the possibility of standardization of the so-called plasma dose.

Subject Index H04, J29

1. Introduction

Due to their electrical and chemical properties, plasma discharges in open air release a unique cocktail of charged species, energetic photons, and active radicals into the surrounding environment. Non-thermal atmospheric-pressure plasma, also termed cold plasma, is defined as a low degree of ionization gas. The interaction of non-thermal plasma with surfaces has been a subject of intense study for many decades. Both atmospheric-pressure plasma and low-pressure plasma have been widely used to modify and functionalize a large variety of surfaces including polymers and biomaterials [1–5]. The physical understanding of boundary surface–plasma interaction processes has become a subject of fundamental importance [6]. The depth up to which the different processes affect the surface typically range from 1 nm (functionalization) to 10–100 nm (etching), and up to 1 μm for coatings. In practice the different processes are often not separated, but occur simultaneously, e.g. cleaning may include sputtering or functionalization, or etching may occur along with deposition and/or sputtering.

For biological applications, the temperature of the plasma should be maintained as low as possible and operational pressure should be atmospheric, to prevent or minimize detrimental effects. The electrons in the discharge have a temperature of a few eV, but the gas should remain at room temperature or slightly above. To achieve such a goal, the design of cold atmospheric plasma devices should enhance heat loss and reduce the applied power. A reduction in the heat loss can be achieved by using reduced plasma surface to volume ratios, while low operating powers can be achieved by reducing the operating voltage (lowest breakdown voltage for helium and argon). At least three different principles of generating non-thermal plasmas at atmospheric pressure have been developed for biomedical applications [7]: plasma jets, corona discharge plasma sources, and dielectric barrier discharge plasma sources. In this work, a commercially available plasma jet named KinPen MED^{TM} [8,9] with pure argon as a carrier gas is used.

A major component of this work is optical emission spectroscopy (OES) for the diagnostics of the plasma discharge. OES is based on analyzing the light emitted by neutral or ionized atoms, radicals, or molecules; the technique is widely used as a diagnostic tool in plasma processing. OES can be used for excited species characterization, photon flux determination as a function of wavelength, for actinometry, and as a diagnostic for electron beams. Advantages of using OES are: (i) it is non-intrusive; (ii) a large excitation cross section produces a strong signal; (iii) emission from optically allowed states is insensitive to beam energy; (iv) a short lifetime facilitates a good temporal response and fewer complications from quenching; (v) a large excitation energy minimizes the excitation caused both by "plasma" electrons and the radiative cascade; and (vi) data interpretation is direct and relatively simple when quenching and photon re-absorption (within the medium and outside) are weak (however both effects can be included if necessary).

In this work the plasma jet only uses pure argon, however the plasma chemistry is a mixture of argon–nitrogen–oxygen. That is, an open-air plasma discharge is always affected by the ambient air chemistry [10]. Based on the ionization rate for atmospheric plasma discharges, most of the plasma energy is spent on the production of optically allowed states, forbidden states (metastables), and dissociation. Most metastables have long lifetimes, and thus the metastable population can grow to high levels. Strong emissions from excited neutral atoms are predominant for argon (Ar I). The optical emission comes mainly from depopulation of the 4p levels via multiple 4p–4s transitions, including coupling of the most prominent argon atomic transition: $4p[5/2]_3 \rightarrow 4s[3/2]_2$ for $\lambda = 811.531$ nm (Ar811) and $4p'[1/2]_0 \rightarrow 4s'[1/2]_1$ for $\lambda = 750.387$ nm (Ar750) [11]. Emission from atomic ions was not evident. The dominant nitrogen emission was the band emission of the molecular nitrogen ion from the first negative system $N_2^+ \left(B^2\Sigma_u^+ \rightarrow X^2\Sigma_g^+\right)$ with the dominant emission line at $\lambda = 391.44$ nm (vibration quantum numbers $v' = 0 - v'' = 0$) [12–14]. Due to the high energy threshold for this reaction ($E_{th} = 18.8$ eV), high-energy electrons are the main contributors to molecular ion production. The other option for this reaction is collisions with metasable atoms. Only helium metasable atoms have enough energy [11], i.e. more than the energy threshold for this reaction, and helium is not part of our chemistry. For the nitrogen molecule, direct excitation of neutrals $\left(e_{fast} + N_2 \rightarrow N_2^* + e_{slow}\right)$, is the second dominant process. In particular, band emissions from the first positive $\left(B^3\Pi_g \rightarrow A^3\Sigma_u^+, E_{th} = 7.35\,\mathrm{eV}\right)$ and the second positive $\left(C^3\Pi_u \rightarrow B^3\Pi_g, E_{th} = 11.03\,\mathrm{eV}\right)$ [12–14] systems were detected. The threshold levels for excitation are much lower than for the charged species, and thus the influence of low-energy electrons on their production is more significant. Oxygen species were studied in the argon plasma using measurements of atomic (O I) spectral emissions. The recorded atomic oxygen spectral lines are triplets [11] at $\lambda = 777$ nm (O777) and at $\lambda = 845$ nm (O845). The spectral emission of molecular oxygen and the spectral emission that comes from the high-lying excited energy levels of atomic oxygen are very weak.

As mentioned above, many different atomic and molecular electronic transitions take place in the plasma. Thus is due to the energy threshold for the transition, the chemical properties of the emitter, the mechanisms for creation of the excited energy states, etc. This study is focused on all of these parameters. Starting with an investigation of the influence of the gas flow rate on the spectral emissions, follow by mapping the plasma spectral intensity distribution as a function of the distance and processing time. Special attention is paid to argon spectral radiation with respect to the metastable density in a confined open-air plasma discharge. This approach is presented for the first time for monitoring the density of argon metastable atoms by OES. Oxygen and nitrogen radicals from ambient air play a critical role in atmospheric plasma chemistry, and in some cases they are unwanted chemistry. Therefore, one of the objectives of this work is to explore the temporary and spatial production of oxygen and nitrogen species in the argon plasma jet discharge. Finally, a change in the electron energy distribution function (EEDF), as a function of gas flow rate, distance, and processing time, in the argon–air plasma is monitored. It is important to note that there are two sets of spectral lines recorded in this work, regardless of the radiator. The first are the upper energy states populated by direct electronic (high-energy electrons) collisions with the atom in the ground state. The second are created in collisions between low-energy electrons and argon metastable atoms. The resultant ratios between such spectral emissions are employed to determine the EEDF.

2. Experiment

Experiments were conducted with the commercially available KinPen MED$^{\mathrm{TM}}$ [8,9] shown in Fig. 1. From an optimization study perspective the system is limited due to its closed-box design, with the plasma generator and its matching network housed in a close unit, consequently limiting plasma diagnostics to optical-based techniques only. The KinPen MED$^{\mathrm{TM}}$ sources consist of a hand-held unit for the generation of a plasma jet at atmospheric pressure, an RF power supply, and a gas supply unit which operates with all noble gases, along with nitrogen and air, and admixtures of molecular gases to the nobel gas. The plasma is ignited at the tip of a centered electrode inside a capillary and blown out by the gas flow. Because of the contracted plasma resulting from this type of generation, the KinPen MED$^{\mathrm{TM}}$ is especially suited for focused treatment of small areas. Large-scale treatments can be realized by moving the jet by a computer numeric control (CNC) machine over a selected area. The CNC is included in this work, and is used for OES measurement of the atomic and molecular absolute spectral emissions of argon, oxygen, and nitrogen. Analysis of these species' spectral intensities will assist in the development of optimized plasma processing parameters for biological treatments.

The plasma applicator is mounted on a CNC, the speed of which can be set at up to 250 mm s^{-1}. The system power is 8 W at 220 V, 50/60 Hz. In the center of a quartz capillary (inner diameter 1.6 mm), a pin-type electrode (1 mm diameter) is mounted. In the continuous working mode, a high-frequency voltage (1.1 MHz, 2–6 kVpp) is coupled to the pin-type electrode. The plasma is generated from the top of the central electrode and expands to the surrounding air outside the nozzle. The argon flow rate is changing from 1.3 L min^{-1} to 5.0 L min^{-1}. The argon gas velocity during this experiment was calculated to be between 0.2 and 0.7 m s^{-1} and has a laminar flow with a Reynolds number around 100. The system could support higher gas flow rates; however, the use of argon at high flow rates can create unstable plasma discharges. That is, for higher argon gas flow rates, mixtures of nitrogen, oxygen, and argon could easily cause the transition from a stable homogeneous discharge into a filamentary discharge. Consequently, argon gas flow rate is kept below 5.0 L min^{-1}. Oxygen and nitrogen come for the ambient air and are not controlled, but through the approach used in this experimental design their impact can be limited.

The transfer of radiation throughout inhomogeneous plasmas has a significant impact on the spectral line's shape and overall intensity. Optically thin conditions must prevail at the line centers, or appropriate corrections must be made when using OES data for quantitative analysis [15]. Several

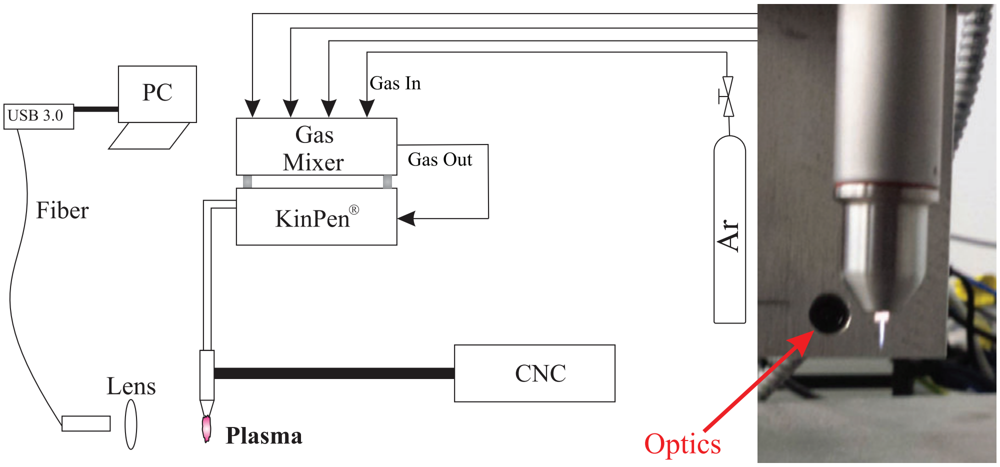

Fig. 1. Photograph of KinPen MED$^{\mathrm{TM}}$ plasma source (right) with the schematic of the whole system (left).

techniques exist for determining the effect of self-absorption. The most straightforward method is to check line intensity ratios within multiplets which abide by the so-called LS-coupling rules [16]. The reduction in the observed intensity of the strongest or metastable line within the multiplet, in respect to the weakest spectral line in the same multiplet, shows that self-absorption is present. A variation of this technique is to vary the concentration of the species under study and then to observe variations in the intensity ratio with decreasing concentration. If the spectral line ratio remains constant within the lines' multiplet these plasmas are considered optically thin and do not require any correction for self-absorption. The theoretical line ratios are calculated using Eq. (1) [15]:

$$S = \frac{g_{k1} \cdot \lambda_1^3 \cdot A_{ki1}}{g_{k2} \cdot \lambda_2^3 \cdot A_{ki2}}, \tag{1}$$

where g_k is the upper level statistical weight, λ is the wavelength, and A_{ki} is the transition probability value. The selected spectral line ratios are the ratios between the high-intensity spectral lines and the lower-intensity spectral lines or the ratio between spectral lines for which the lower energy level is the metastable and the lowest intensity from the multiplet. Any deviations between experimental and theoretical data are taken as indications of self-absorption within that multiplet. The scale of the plasma in this work is quite limited and the opacity effect of the plasma is not recorded.

Optical emission spectroscopy was carried out using an Edmund Optics UV-VIS Enhanced Smart CCD Spectrometer. The spectrometer has a linear CCD chipset, with a wavelength range sensitivity of 200–875 nm and spectral resolution of 1.8 nm. Light from the plasma passes through a focusing lens and a 2 m-long 400 μm multi-mode fiber optic cable. The OES technique is based on the integration of measured signals over a line-of-sight observation. Experiments were carried out to investigate species' spectral intensities with varying argon flow rate, distance, and processing time. The processing time, i.e. the time sequence of the recorded spectrum, was every 10 seconds for a duration of 3 minutes. The plasma jet was used without any samples, so the processing time will help monitor fluctuations in the plasma spectral emission. In order to collect spatial and temporal OES data by covering the multivariate process space and evaluate the cross-dependencies of the measured outputs, a comprehensive design of experiment (DOE) approach was taken. This resulted in a matrix of 164 experiments, in contrast to the approach without DOE that gives a total number of experimental runs of 2232. In order to truly establish species importance at the various processing

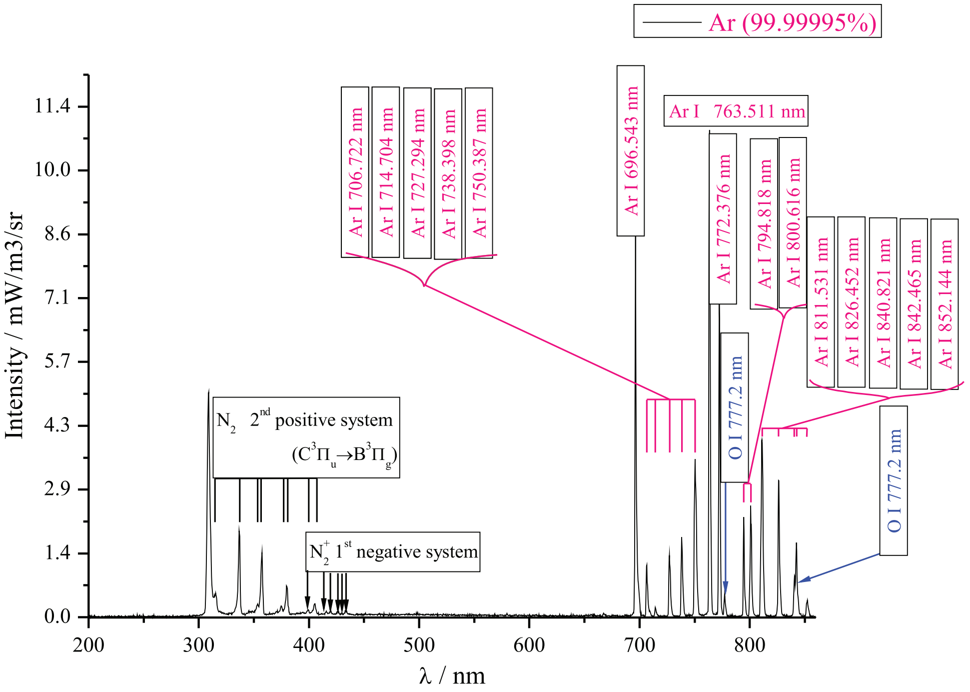

Fig. 2. Spectrum of atomic argon (the most important spectral lines are labeled) with addition of oxygen and nitrogen from an ambient air, for the argon plasma jet discharge recorded 10 s after the plasma was struck, with an argon flow rate of 2.5 L min^{-1} and 3 mm from the jet nozzle.

parameters, it was necessary to integrate the area under the emission peaks [17] for each OES spectra and to calculate a quantum efficiency of the spectral system (the spectrometer, fiber optic cable, lens, etc.). The areas under the emission peaks, shown in Figure 2, were measured and expressed in units of mW cm^{-3} sr^{-1} for a 1 second integration time. The low resolution of the spectrometer has no significant influence on the profile's separation and the recorded continuum emission is very low. The low continuum emission indicates that the gas temperature is not high, i.e. it is not drastically different from the ambient temperature. In order to compare recorded spectra calibration of optical detection system, i.e. a calculation of the quantum efficiency, is done. The system's quantum efficiency was determined as for the method of Ref. [18] using a 20 W tungsten–halogen calibration light source (Edmund optics).

The calibration of the optical detection system is a determination of its quantum efficiency, i.e. measurement of the quantum efficiency of the system versus wavelength. In principle two kinds of calibrations could be performed, one relative and the other absolute. When the calibration standard has a spectral radiance in dimensionless units then a relative calibration can be employed, otherwise it is possible to have absolute calibration. A standard lamp is a light source which represents an approximation of a black body. The intensity measured by a spectrometer, dependent on wavelength (λ), is given by

$$I_\lambda^{\mathrm{Spec}} = I_\lambda^{\mathrm{Sour}} \cdot \Omega_{\mathrm{eff}} \cdot \Delta A \cdot \Delta\lambda \cdot T_{\mathrm{F}} \frac{\lambda}{h \cdot c} \cdot T_{\mathrm{W}} \cdot Q_\lambda. \tag{2}$$

where $I_\lambda^{\mathrm{Sour}}$ is intensity of the light source dependent on the wavelength, Ω_{eff} is the effective spatial angle, ΔA is the effective area of the source, Δλ is the spectral interval, T_F is the transparency of the interference filter, T_W is the transparency of the window on the light source, and Q_λ is the quantum efficiency of spectrometer.

Table 1. Spectroscopic data of the relevant atomic argon (Ar I) emission spectral lines. The transition energy levels are based on Racah notation (first column), L–S notation (second column), and Paschen notation (third column), wavelengths, relative intensity, initial energy levels (E_i) and final energy levels (E_f), are taken from Ref. [11].

λ (nm)	Transition			Rel. Intensity (a.u.)	E_i (eV)	E_f (eV)
696.543	$4p'\ ^2[1/2]_1 \rightarrow 4s\ ^2[3/2]^o_2$	$^1P_1 \rightarrow {}^3P_2$	$2p_2 \rightarrow 1s_5$	10000	13.33	11.55
706.722	$4p'\ ^2[3/2]_2 \rightarrow 4s\ ^2[3/2]^o_2$	$^3P_2 \rightarrow {}^3P_2$	$2p_3 \rightarrow 1s_5$	10000	13.30	11.55
714.704	$4p'\ ^2[3/2]_1 \rightarrow 4s\ ^2[3/2]^o_2$	$^3P_1 \rightarrow {}^3P_2$	$2p_4 \rightarrow 1s_5$	1000	13.28	11.55
727.294	$4p'\ ^2[1/2]_1 \rightarrow 4s\ ^2[3/2]^o_1$	$^1P_1 \rightarrow {}^3P_1$	$2p_2 \rightarrow 1s_4$	2000	13.33	11.62
738.398	$4p'\ ^2[3/2]_2 \rightarrow 4s\ ^2[3/2]^o_1$	$^3P_2 \rightarrow {}^3P_1$	$2p_3 \rightarrow 1s_4$	10000	13.30	11.62
750.387	$4p'\ ^2[1/2]_0 \rightarrow 4s'\ ^2[1/2]^o_1$	$^1S_0 \rightarrow {}^1P_1$	$2p_1 \rightarrow 1s_2$	20000	13.48	11.83
751.465	$4p\ ^2[1/2]_0 \rightarrow 4s\ ^2[3/2]^o_1$	$^3P_0 \rightarrow {}^3P_1$	$2p_5 \rightarrow 1s_4$	15000	13.27	11.62
763.511	$4p\ ^2[3/2]_2 \rightarrow 4s\ ^2[3/2]^o_2$	$^3D_2 \rightarrow {}^3P_2$	$2p_6 \rightarrow 1s_5$	25000	13.17	11.55
772.376	$4p\ ^2[3/2]_1 \rightarrow 4s\ ^2[3/2]^o_2$	$^3D_1 \rightarrow {}^3P_2$	$2p_7 \rightarrow 1s_5$	15000	13.15	11.55
772.421	$4p'\ ^2[1/2]_1 \rightarrow 4s'\ ^2[1/2]^o_0$	$^1P_1 \rightarrow {}^3P_0$	$2p_2 \rightarrow 1s_3$	10000	13.33	11.72
794.818	$4p'\ ^2[3/2]_1 \rightarrow 4s'\ ^2[1/2]^o_0$	$^3P_1 \rightarrow {}^3P_0$	$2p_4 \rightarrow 1s_3$	20000	13.28	11.72
800.616	$4p\ ^2[3/2]_2 \rightarrow 4s\ ^2[3/2]^o_1$	$^3D_2 \rightarrow {}^3P_1$	$2p_6 \rightarrow 1s_4$	20000	13.17	11.62
801.479	$4p\ ^2[5/2]_2 \rightarrow 4s\ ^2[3/2]^o_2$	$^3D_2 \rightarrow {}^3P_2$	$2p_8 \rightarrow 1s_5$	25000	13.09	11.55
810.369	$4p\ ^2[3/2]_1 \rightarrow 4s\ ^2[3/2]^o_1$	$^3D_1 \rightarrow {}^3P_1$	$2p_7 \rightarrow 1s_4$	20000	13.15	11.62
811.531	$4p\ ^2[5/2]_3 \rightarrow 4s\ ^2[3/2]^o_2$	$^3D_3 \rightarrow {}^3P_2$	$2p_9 \rightarrow 1s_5$	35000	13.08	11.55
826.452	$4p'\ ^2[1/2]_1 \rightarrow 4s'\ ^2[1/2]^o_1$	$^1P_1 \rightarrow {}^1P_1$	$2p_2 \rightarrow 1s_2$	10000	13.33	11.83
840.821	$4p'\ ^2[3/2]_2 \rightarrow 4s'\ ^2[1/2]^o_1$	$^3P_2 \rightarrow {}^1P_1$	$2p_3 \rightarrow 1s_2$	15000	13.30	11.83
842.465	$4p\ ^2[5/2]_2 \rightarrow 4s\ ^2[3/2]^o_1$	$^3D_2 \rightarrow {}^3P_1$	$2p_8 \rightarrow 1s_4$	20000	13.09	11.62
852.144	$4p'\ ^2[3/2]_1 \rightarrow 4s'\ ^2[1/2]^o_1$	$^3P_1 \rightarrow {}^1P_1$	$2p_4 \rightarrow 1s_2$	15000	13.28	11.83

The effective spatial angle (Ω_{eff}) is defined by the ratio between the effective area of the lens and the square of the distance between the lens and the light source. The spectral interval $(\Delta\lambda)$ is equal to the result of multiplication between the reciprocal dispersion of the monochromator and the width of the exit slit. Using Eq. (2) and with known $I_\lambda^{\mathrm{Sour}}$ and $I_\lambda^{\mathrm{Spec}}$, the quantum efficiency of the spectrometer (Q_λ) can be found:

$$Q_\lambda = \frac{I_\lambda^{\mathrm{Spec}}}{I_\lambda^{\mathrm{Sour}}} \cdot \frac{h \cdot c}{\Omega_{\mathrm{eff}} \cdot \Delta A \cdot \Delta\lambda \cdot T_F \cdot \lambda \cdot T_W}. \tag{3}$$

In this study, 19 argon spectral lines are included and listed in Table 1, with two atomic oxygen spectral triplets from the 3s–3p transition [11]: $^5S^o_2 - {}^5P_{3,2,1}$ (777.194 nm, 777.417 nm, and 777.539 nm) and $^3S^o_1 - {}^3P_{2,1,0}$ (844.625 nm, 844.636 nm, and 844.676 nm), as well as the N_2 second positive [14] $\left(C^3\Pi_u \rightarrow B^3\Pi_g,\ v' = 0 - v'' = 0\right.$, with the main band-head at 337.14 nm$\left.\right)$ and N_2^+ first negative [12] $\left(B^2\Sigma_u^+ \rightarrow X^2\Sigma_g^+,\ v' = 0 - v'' = 0\right.$, with the main band-head at 391.44 nm$\left.\right)$ spectral emissions. The most important of all these argon spectral lines is Ar750, with the energy of the $^2[1/2]_0$ 4p equal to 13.48 eV and a 22 ns lifetime [11]. The Ar750 spectral line is created by direct electron excitation from the ground level [19] and could be a good representative [20] of the ion density in the plasma. From the two oxygen triplets the strongest oxygen spectral emission is O777. The O777 triplet has the common lower energy level and small differences (less than 1%) in the upper energy level ($E_i = 10.74$ eV) [11]. The lifetime of the $3p(^5P)$ state is about 30 ns. The upper and lower energy levels of N_2 337.14 nm spectral emissions have energies of 11.03 eV and 7.35 eV, respectively. In contrast to other metastables, the $C^3\Pi$ state has a natural lifetime of only

45 ns, comparable to that of optically allowed states [13]. The ionization energy of the N_2 molecule is 15.58 eV. Certain argon spectral lines are very close to each other: 750.387 nm and 751.465 nm; 772.376 nm and 772.421 nm; 800.616 nm and 801.479 nm; 810.369 nm and 811.531 nm; 840.821 nm and 842.465 nm [11]. For all of these, the deconvolution procedure of a two-Gaussian function is applied [17].

3. Results and discussion

Figure 3 shows the prediction profile (top) and the interaction profiles (bottom) of the absolute total spectral emission from the plasma as a function of the three external parameters. The spectral emission (Fig. 3) strongly depends on the distance; after that, the argon gas flow rate, and almost not at all on the processing time. No sample was used for these experiments, with the plasma discharged into air to simplify the investigation of the discharge homogeneity and reproducibility. In this case the result of the plasma fluctuation with time shows high reproducibility (more than 99%). Any fluctuations in the radiative emission by addition of a sample to the discharge can be explained by the interaction between the system and the plasma [21]. Distance plays the most important role in the spectrum emission. With increasing distance, the total spectral radiation from the plasma decreases and the maximum of the spectrum distribution (not shown here) shifts from the red toward the blue wavelength. It should be noted that this is the total spectral radiation—the individual radiators from the plasma show different trends (shown below). Finally, the total intensity has a similar functional dependence (but with different slopes) on the gas flow rate and distance. Since the processing time has no impact on the spectral intensity, all results will be presented at 10 seconds after the plasma was struck.

For the argon energy levels used in this study, the lifetime of the resonant energy levels are 8.4 ns $(1s_4)$ and 2.0 ns $(1s_2)$; the lifetime of the metastable energy levels are 50 s $(1s_3)$ and 40 s $(1s_5)$; the electron lifetimes for all other argon energy levels are 30 ns $(2p_9)$, 108 ns $(2p_8)$, 41 ns $(2p_6)$, 25 ns $(2p_3)$, and 22 ns $(2p_1)$ [11]. The lifetime of electrons in resonant, metastable, Rydberg or/and "ordinary" allowed and forbidden excited energy states are determined by many factors which could be quite different from the theoretical values. In plasma the microscopic processes are dominated by collective interactions, in the first place by collisions, and therefore electron lifetimes in the excited states could be shorter or longer. In Eq. (4), the parameters influencing the mean lifetime of a metastable's energy level are presented:

$$1/\tau_m = 1/\tau_i + 1/\tau_d + 1/\tau_r + 1/\tau_q, \tag{4}$$

where τ_i is the radiative lifetime, τ_d is the diffusion time, τ_r is the residence time in the chamber due to pumping, and τ_q is the quenching time. Equation (4) takes into account all effects that could impact on the lifetime of an electron in excited states, from low pressure to open-air plasma discharges. Due to the different gas backgrounds, i.e. argon gas for the plasma inside the nozzle, argon mixed with air molecules (nitrogen and oxygen) for the plasma in open air, the quenching mechanisms for the excited species are different and listed in Ref. [22]. Although air molecules were diffused into the nozzle, which is indicated by the N_2 bands, the air concentration was considered to be very low and would not play an important role in the quenching processes of excited and metastable Ar for the plasma inside the nozzle. The rate coefficient for the quenching process that includes the excited argon atom and ambient gas in the nozzle is $\sim 10^{11}$ cm^3 s^{-1} and outside the nozzle $\sim 10^{11}$–10^{10} cm^3 s^{-1} [23]. Due to the high quenching rates by N_2 molecules, the excited argon, oxygen, or OH states will vanish

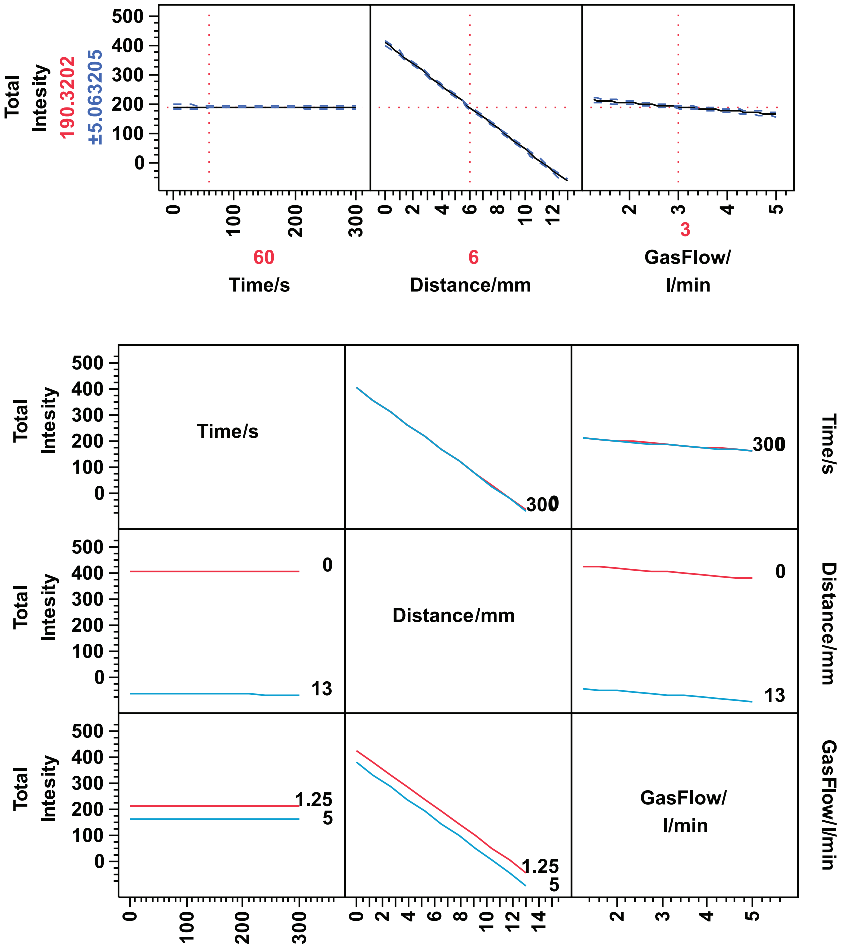

Fig. 3. DOE screening. Absolute total spectral intensity (from 200 nm to 875 nm) in mW m^{-3} sr^{-1} as the function of processing time, distance, and argon gas flow rate.

quickly and result in a rapid decay in the corresponding emission intensity if the N_2 concentration is high (i.e. outside the nozzle) [24].

One approach to understanding cross-linkage among plasma species is to produce an energy diagram of the spectral emission. The energy diagram (Fig. 4) takes into account the energy levels of the most important spectral profiles emitted in the plasma (Fig. 2), and also helps to predict a possible resonant energy transfer among the different plasma species. Those resonant energy transfers are non-radiative and important for plasma diagnostics. One of the brightest argon lines in the wavelength range 700–890 nm occurs at 750.4 nm. The emissions at 104.8 and 106.7 nm are even brighter, but those resonate spectral lines that lie outside the range of the spectrometer used in the experiments. The energies of those photons exceed 11 eV, enough to modify a material's chemistry and morphology. From the argon spectral lines in Fig. 2, most have transition to the resonant $1s_2$ and $1s_4$ (in Paschen's notation), or the metastable $1s_3$ and $1s_5$ energy levels. The lifetimes of electrons in the resonant energy levels are much shorter than in an "ordinary" excited energy level and are many orders of magnitude shorter than an electron's lifetime at metastable energy levels. In general, the quenching of resonant energy levels is negligible and therefore an electron transition (e.g. Ar750) that ends on a resonant energy level may be used for monitoring an atom's density in its ground state. Argon metastable energy levels have lifetimes over 1 s, consequently they act as a "reservoir

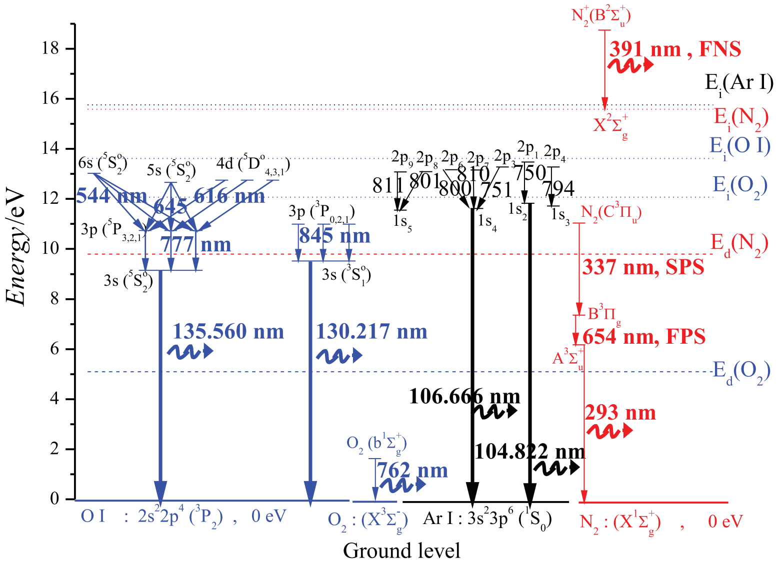

Fig. 4. Simplified energy diagram for excited species in an argon–nitrogen–oxygen mixture. The acronyms FNS $(v' = 0 - v'' = 0)$, FPS $(v' = 7 - v'' = 4)$, SPS $(v' = 0 - v'' = 0)$ denote first negative, first positive, and second positive molecule nitrogen systems respectively. E_d is dissociation and E_i is ionization energy.

of energy." One of the ways to gain an insight into the argon metastable density is to record the spectral emission from "all" lines for which the lower energy level is the metasable. From the 19 recorded argon spectral lines, the following ones are used for monitoring the metastable argon atom in the $1s_5$ state: 696.543 nm, 706.722 nm, 714.704 nm, 763.511 nm, 772.376 nm, 801.479 nm, and 811.531 nm. In addition, the emissions at 772.421 nm and 794.818 nm are used for monitoring the metastable argon atom in the $1s_3$ state.

Plasma kinetics at an atmospheric pressure could be impacted by quenching among the argon metastable and resonant levels. There is a small energy difference between argon 4s excited energy states, as the gas is under high pressure, an estimation of so-called collisional mixing should be performed. The four excited states of the Ar 4s level can be quenched by argon through both two-body and three-body quenching reactions [25]. The quenching coefficients for the two-body argon reactions for $1s_5$, $1s_4$, $1s_3$, and $1s_2$ are 0.126, 2.41, 0.319, and 3.07 $\left(\times 10^{-10}\,\mathrm{cm}^3\,\mathrm{s}^{-1}\right)$, respectively. In the case of the three-body quenching reactions the coefficients for $1s_5$, $1s_4$, $1s_3$, and $1s_2$ are 2.17, 2.54, 3.01, and 0.942 $\left(\times 10^{-15}\,\mathrm{cm}^3\,\mathrm{s}^{-1}\right)$, respectively [26,27]. The rate coefficient $1s_3$ to $1s_2$ transfer is found to be $9 \times 10^{19}\,\mathrm{cm}^3\,\mathrm{s}^{-1}$ for a low-pressure system, with a linear dependence on the pressure; however, it can be extrapolated to atmospheric pressure [28]. At atmospheric pressure this constant should be close to the value for the three-body quenching reactions and five orders of magnitude smaller than the two-body quenching reactions. The electron-impact cross sections for the transfer between the excited states of argon, from the metastable $1s_5$ and $1s_3$ states to their respective neighboring resonance states $1s_4$ and $1s_2$, σ_{5-4} and σ_{3-2}, are calculated by the semi-relativistic R-matrix method [29]. The shapes of the $1s_5 \rightarrow 1s_4$ and $1s_3 \rightarrow 1s_2$ transfer cross sections calculated by this method appear very similar. However, a close look at the corresponding curves reveals cross sections at 1 eV of about 12 and 25 $\times\, 10^{20}\,\mathrm{m}^2$ for σ_{5-4} and σ_{3-2}, respectively, leading to a two times larger rate coefficient for the $1s_3 \rightarrow 1s_2$ transfer. This tendency for a 2 to 4 times larger σ_{3-2}, compared to σ_{5-4}, is also observed in the rate coefficients $1s_3$ to $1s_2$ and $1s_5$ to $1s_4$, respectively. Thus, the main mechanism of excite/de-excite of argon 4s energy states is direct electron excitation from the

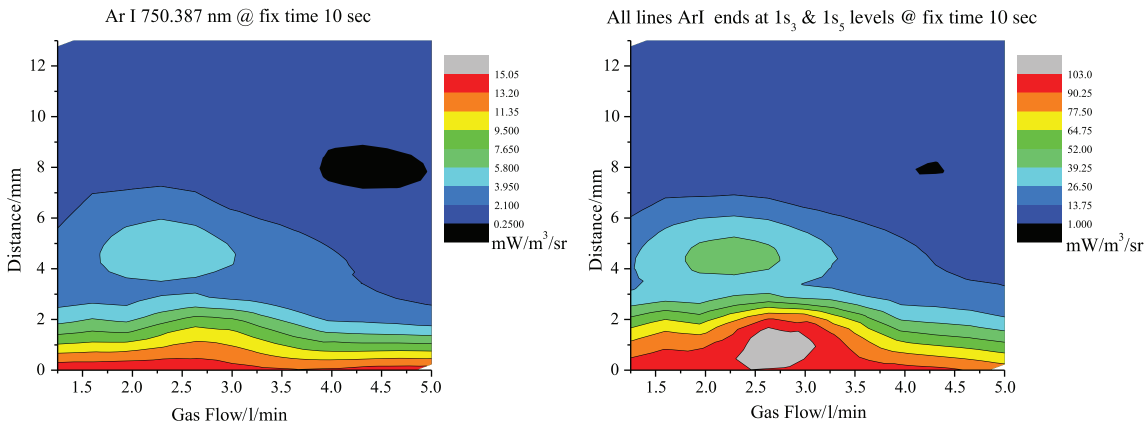

Fig. 5. Absolute spectral emission of Ar750 (left) and the nine atomic argon spectral lines which end on one of two argon metastable energy levels, i.e. $1s_3$ or $1s_5$ (right). The ordinate axis is distance from the nozzle of the plasma jet. On the abscissa axis is the argon gas flow rate.

ground level and deactivation of the Ar(4p) state. The Ar(4p) states can only relax into Ar(4s) states by radiative emission. Deactivation of Ar(4p) to the ground state is improbable and does not occur appreciably [30]. One possible experimental validation (apart from an expensive laser absorption system) is recording spontaneous spectra radiation from Ar(4p) states to Ar(4s) states and monitoring the transition branch ratio. For example, line intensities for transitions from $2p_2$ to $1s_2$ ($\lambda = 826.5$ nm), from $2p_2$ to $1s_3$ ($\lambda = 772.4$ nm), from $2p_2$ to $1s_4$ ($\lambda = 727.3$ nm), and from $2p_2$ to $1s_5$ ($\lambda = 696.5$ nm) are in the ratio of 42.6 : 33.1 : 5.1 : 19.2, respectively [11]. Our measurements show, on average, a 3% intensity deviation from these values. The transition branch ratio was tested for other argon spectral lines from the $2p_3$, $2p_4$, $2p_6$, $2p_7$, and $2p_8$ energy states, but not for $2p_1$, $2p_5$, and $2p_9$ levels because only one spectral line from each of these energy states was recorded.

Figure 5 shows the absolute argon spectral distributions as a function of the gas flow rate and distance. The Ar750 distribution is almost constant with flow rate (the fluctuation of intensity is about ±2%), but is drastically changing with distance. On the contrary, for the nine recorded argon spectral lines with the lower energy levels of $1s_3$ or $1s_5$ (metastable levels), the spectral distribution shows significant fluctuation with the gas flow rate and even greater fluctuation with distance (see Fig. 5, right). Individually, each of the nine spectral lines shows exactly the same spectral distribution pattern (not shown here) as for the combined lines (Fig. 5, right). This spectral distribution has, in this two-dimensional space, one distinguished maximum at a $2.7\,\mathrm{L\,min^{-1}}$ flow rate and a distance of 1 mm.

As mentioned above, the main kinetic processes of Ar(2p) levels are the electron-impact excitation from the 1s levels and the electron-impact and atom-collision population transfer. When the electron density is very high ($>10^{17}\,\mathrm{cm^{-3}}$), the electron-impact population transfer is the dominant depopulation process. As a result, the Ar(2p) levels have a Boltzmann-like population distribution, and the densities of $\mathrm{Ar}\left(2p_2\right)$ and $\mathrm{Ar}\left(2p_3\right)$ $\left(n_{2p2}, n_{2p3}\right)$ are similar due to the similar electron-impact excitation and depopulation rate coefficients. When the electron density is low $\left(<10^{11}\,\mathrm{cm^{-3}}\right)$, the atom-collision population transfer becomes the dominant depopulation process. As a result, the Ar(2p) levels have an extremely non-equilibrium distribution with $n_{2p2} >> n_{2p3}$, since the atom-collision depopulation rate coefficient of $\mathrm{Ar}\left(2p_2\right)$ is much smaller than that of $\mathrm{Ar}\left(2p_3\right)$. The ratio of n_{2p3} to n_{2p2} increases significantly with n_e. Therefore, n_e can be obtained from their line-ratios. On the other hand, the mean electron energy can be determined from the line-ratio of the Ar lines by considering the different electron-impact excitation threshold energies of Ar 2p levels [31]. In this work the electron density obtained from the measured line-ratios of Ar(2p) levels, according to an atmospheric-pressure collisional–radiative model [32], is 1.4×10^{11} cm^{-3}. This is the maximum value for a distance of 0 mm and gas flow rate of 2 L min^{-1}.

Argon has no excited states below 11.55 eV and thus below this energy elastic collisions are the only electron cooling mechanism. Since this experiment does not concern pure argon plasma, other species like oxygen and nitrogen could have non-radiative energy transfer with excited argon atoms. Oxygen and nitrogen have energy states below this "threshold" of 11 eV. Oxygen lacks electronic states between 6.1 and 9.14 eV, while nitrogen has electronic states up to the ground level.

The rotational temperature (T_r) of molecular nitrogen FPS becomes lower as the plasma flows away from the nozzle, since the collisional relaxation becomes essential. In particular, when the discharge pressure increases [33], the rotational temperatures both of FPS and of SPS are almost the same throughout the observed domain over the plasma discharge. The pressure (as high as atmospheric) can enhance the collisional relaxation, and consequently both rotational temperatures are considered to agree very well with each other. Basically, the rotational constant of the nitrogen molecules is very small, not only for the ground state X $^1\Sigma_g^+$ but also for the excited states B $^3\Pi_g$, C $^3\Pi_u$, etc. Therefore, the rotationally excited levels can frequently exchange kinetic energy with the translational motion of neutral nitrogen molecules. Consequently, it is considered that the energy distribution of rotational levels is almost equilibrated with that of translational motion through a few collisions. On the other hand, the vibrational temperature (T_v) of FPS is significantly lower than that of SPS [34]. However, the dependence on the discharge pressure is qualitatively similar, i.e., the vibrational temperature tends to decrease as the discharge pressure increases. This can also be attributed to the frequent collisional relaxation with neutral molecules. The discrepancy on vibrational temperatures between FPS and SPS can be explained by the dominant molecular processes for the excitation and de-excitation of the upper state of FPS and SPS, that is, B $^3\Pi_g$ and C $^3\Pi_u$. Basically, the rotational motion of the molecular species in the plasma is considered to be an approximate value of the gas translational temperature, which is the case for N_2 C $^3\Pi_u$ and B $^3\Pi_g$ states as already shown [35]. However, the rotational temperature of FNS is higher than those of FPS and SPS, and consequently it does not correspond to the translational temperature of neutral molecules [36]. That experimental result possibly indicates that the dominant population process of excited states B $^2\Sigma_u^+$ of N_2^+ is not the direct excitation from the ground state of the neutral N_2 molecule, or from the excited states of the neutral molecular state. Otherwise, the rotational energy distribution of N_2^+ B $^2\Sigma_u^+$ should become almost the same as the initial state of the molecule. One possible reason for the higher T_r of FNS is that the predominant population process of the B $^2\Sigma_u^+$ of N_2^+ ion is the electron impact excitation from the ground state X $^2\Sigma_g^+$ of the N_2^+ ion and not from any state of the neutral molecules. Then, the rotational energy distribution of B $^2\Sigma_u^+$ of N_2^+ should be close to that of the ground state X $^2\Sigma_g^+$ of the N_2^+ ion. The variation in the rotational temperature is considered to be useful for the analysis of the macroscopic thermal structure of nitrogen plasma, which is mostly determined by the temperature of the neutral particles [33,34,37]. The vibrational temperature is much higher than the rotational temperature, since the vibrational kinetics are considerably determined by the electron impact excitation. The vibrational temperature decreased with increasing discharge pressure. It is considered that the collisional relaxation of molecules proceeds rapidly at higher discharge pressure [38,39].

The admixture of nitrogen and oxygen with lighter rare-gas species (e.g. helium) increases the electron temperature, since the lighter rare-gas species have higher ionization potential [40]. On the other hand, the heavier rare-gas species (e.g. argon) have lower ionization potential, and consequently the

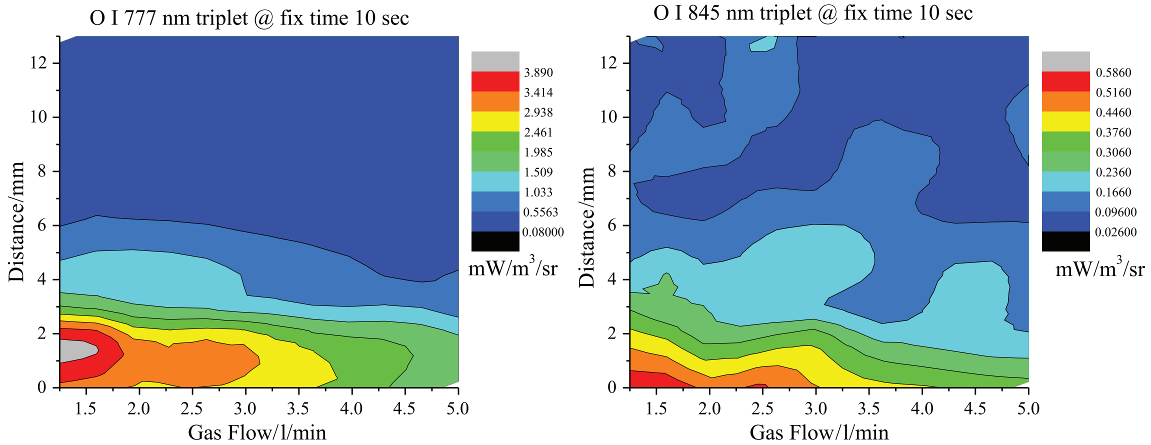

Fig. 6. Absolute spectral emission of O I at 777 nm (left) and O I at 845 nm (right). The ordinate axis is distance from the nozzle of the plasma jet. On the abscissa axis is the argon gas flow rate.

electron temperature can become lower and the electron density increases with increasing volumetric ratios of the heavier rare-gas species. When argon, with lower ionization energy, is mixed into the nitrogen-rich plasma, it is found to lower the electron temperature with a resultant reduction in the degree of nitrogen dissociation. For these three kinds of rare gases, the variation in their dissociation degree is reasonable since it corresponds to the variation in the electron temperature [41].

The spectral emission of nitrogen and oxygen species comes from the ambient air and shows a strong link with the emission pattern of the argon atom. Figure 6 shows the atomic oxygen spectral distribution as a function of gas flow rate and distance.

Both spectral emissions (O777 and O845) have a similar spectral "fingerprint." Their spectral radiations are significant only for the low argon gas flow rate and for the first 2–3 mm from the nozzle. The production of excited oxygen atoms depends quadratically on the plasma density. The upper energy levels for both emissions can be populated by the direct electron impact (excitation process) from the ground state of the O I. Therefore these spectral emissions have a similarity with the Ar750 (significant spectral radiation only up to 3 mm from the nozzle). The other competing process for the creation of O777 and O845 emission is excitation by molecular dissociation. This process is more significant for O777 than O845 due to the higher cross section for excitation by molecular dissociation. The excitation process occurs with the oxygen molecule by physical quenching, and only results in the deactivation of singlet oxygen to its ground state, with no oxygen consumption or product formation. Molecular oxygen has a molecular band around 762 nm (a band center), which belongs to a vibrational subtransition of the $b^1\Sigma_g^+ \to X^3\Sigma_g^-$ magnetic dipole transition [42,43]. The R13Q14 line located at 760.26 nm was used to monitor molecule oxygen in this experiment. This line was chosen because it has one of the higher line strengths for the transitions in this region. Although this emission was very weak, it was still detectable, indicating that molecular oxygen contribution most likely has more impact on O777 than O845 emission (that explains some differences in the spectral emissions of O777 and O845 for the low gas flow rate). Nevertheless, with the higher argon gas flow rate, the significance of molecular oxygen and oxygen radicals drops. There is one more channel to explore for creation of O777 and O845 and that is the influence of argon metastable atoms. With the increase in the gas flow rate, the speed of argon atoms increases and energy transfer (quenching) between argon and oxygen is reduced due to the mismatch in their velocities. Distance also has an impact on the energy transfer between these two atoms. The concentration of oxygen in ambient air is constant, at the same time the density of argon metastable atoms significantly drops as a function of jet distance.

The nitrogen molecule has a number of electronic excitation states below the argon metastable energy levels. In this work the strongest N_2 emission was the second positive system $\left(C^3\Pi_u^+–B^3\Pi_g^+\right)$ that dominates the spectral region between 300 and 490 nm. The energies of the excited states are between 9 and 11.5 eV. The corresponding vibration band-heads, $v = 0$, $v = 0, 1, 2, 3$ are located at wavelengths 337, 358, 380, and 406 nm, respectively. Also identified was the spectrum of the N_2^+ first negative system (FNS). The FNS originates from the transition between the excited sates of the molecular ion N_2^+ $B^2\Sigma_u^+$ and the ground state ion N_2^+ $X^2\Sigma_g^+$. It is found near the UV region through to the shorter visible wavelength range, from 320 to 450 nm, which almost overlaps the SPS spectrum. The energy level of the N_2^+ $\left(X^2\Sigma_g^+\right)$ ground state is 15.58 eV, and for the N_2^+ $\left(B^2\Sigma_u^+\right)$ state is 18.75 eV. The $C^3\Pi$ state thus radiates strongly at 337 nm, although not as strongly as the $B^2\Sigma$ ion at 391 nm. This is generally true only if there is sufficient energy to excite such high-lying N_2^+ $B^2\Sigma_u^+$ states. Such states are difficult to reach for argon-dominant plasmas and generally only electrons from the tail of the EEDF can be excited at such energy levels. Consequently, in this work, a very modest signal at wavelength 391 nm is recorded. There is one more spectrum of nitrogen that could have significant spectral radiation, namely the N_2 FPS, whose transition appears between the electronic states $B^3\Pi_g$ and $A^3\Sigma_u^+$. The emission spectrum of FPS is found in the wide wavelength region from 500 nm to 1100 nm, with the strongest band-heads at 580 and 654 nm. In this experiment FPS has negligible spectral emission due to significant discrepancies between the energy of argon metasable levels ($1s_3$ or $1s_5$) and N_2 $B^3\Pi_g$ (7.3 eV). In such cases (over 4 eV energy differences), non-radiative energy transfer is found to be not so effective.

The left graph in Fig. 7 shows a similar spectral distribution as those of the argon spectral lines from Fig. 5 (right). It is well known that the N_2 $C^3\Pi_u^+$ state is populated by quenching with metastable atoms from the noble gas. In these two graphs the spectral emission is proof of non-radiative energy transfer between argon metastable atoms and the nitrogen molecule. At the same time, this validates our approach for estimating the argon metastable density by recording spectral emission of most of the argon lines that end on the $1s_3$ or $1s_5$ energy levels. In the case that our approach is incorrect, one would expect the spectral pattern for N_2 and Ar811, etc., to be different. The other spectral distribution [Fig. 7 (right)] shows a different spectral patterning than N_2. The N_2^+ $B^2\Sigma_u^+$ energy state is populated by a direct electron excitation from the ground state and consequently there is similarity with the spectral emission of Ar750 [Fig. 5 (left)]. At the same time, there is a difference between these two (A750 and N_2^+) spectral emissions. The difference is due to the energy required for the excitation of the N_2^+ $B^2\Sigma_u^+$ and Ar I $4p'[1/2]_0$ energy states. To populate the N_2^+ $B^2\Sigma_u^+$ state only high-energy electrons from the tail of EEDF have sufficient energy levels. Such electrons are accessible only at close proximity to the tip of the nozzle.

Apart from argon metastable atoms and Penning ionization, the EEDF plays an important role in the plasma kinetics of the jet's plasma. The Ar750 spectral line is created by direct electron excitation from the ground level and is sensitive to the high-energy electron portion of the EEDF; on the other side, production of the Ar811 line is sensitive to low-energy electrons. A change in the ratio between Ar811 and Ar750 spectral emissions indicates the change in the EEDF (see Fig. 8). The shift in the dominant argon emission from 811.5 nm to 750.4 nm presumably occurs because of changes in the EEDF. The shift means that the intensity of one spectral line decreases and that of another spectral line increases. That is because of the very large difference in electron energy threshold between excitation out of the ground (13 eV) and of the metastable/resonance levels (2 eV). The excitation rates from

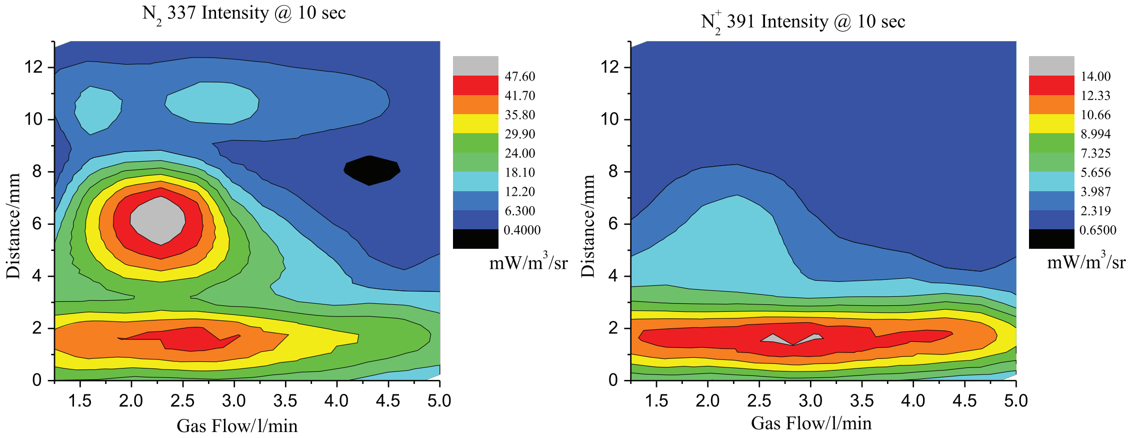

Fig. 7. Absolute spectral emission of N_2 at 337 nm (left) and N_2^+ at 391 nm (right). The ordinate axis is distance from the nozzle of the plasma jet. On the abscissa axis is the argon gas flow rate.

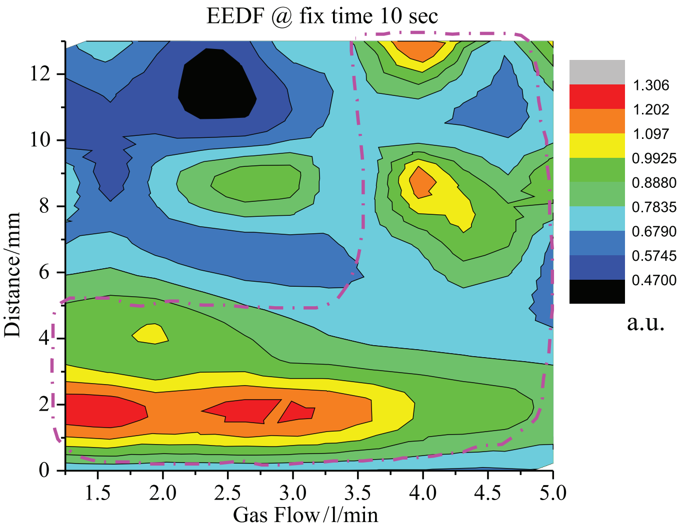

Fig. 8. The shift in electron energy distribution function (EEDF) as a function of the distance from the nozzle of the plasma jet and the argon gas flow rate. The dot-dashed line represents the part of the distribution with the maximum value.

the different initial states sample different segments of the EEDF. This can be seen by examining the energy dependence of the integrand for excitation out of the ground state and the corresponding expression for excitation out of the metastable/resonance level for the $2p_9 \rightarrow 1s_5$ (Ar811) emission and for the $2p_1 \rightarrow 1s_2$ (Ar750) [44]. Several EEDF forms make use of the notion of temperature and are good representations of measured EEDFs under certain discharge conditions. In the case of a "bi-Maxwellian" form, the EEDF is divided into two regions according to electron energy, with the low-energy or "bulk" electron population and higher-energy "tail" of the distribution characterized by different respective temperatures [45,46]. The widely used functional form for the EEDF is the two parameter (x, T_x) function [47–49]:

$$f_{e-x}(E) = c'_1 \cdot T_x^{-3/2} \cdot \sqrt{E} \cdot e^{-c'_2 \cdot (E/T_x)^x}, \tag{5}$$

where

$$c'_1 = x\left(\frac{2}{3}\right)^{3/2}\frac{[\Gamma(5/2x)]^{3/2}}{[\Gamma(3/2x)]^{5/2}}, \tag{6}$$

$$c'_2 = x\left(\frac{2}{3}\right)^{x}\left[\frac{\Gamma(5/2x)}{\Gamma(3/2x)}\right]^{x}, \tag{7}$$

with $\Gamma(w)$ being the Gamma function of w. The Maxwell–Boltzmann distribution is a sub-category of this form that corresponds to the case of $x = 1$ with $c'_1 = 2\pi^{1/2}$ and $c'_2 = 1$. The Druyvesteyn distribution corresponds to the case of $x = 2$ with $c'_1 = 0.5652$ and $c'_2 = 0.2432$. Note that T_x corresponds to an effective temperature $T_x = (2/3)\langle E\rangle$, where $\langle E\rangle$ is the average electron energy, $\langle E\rangle = \int_0^\infty E \cdot f_{e-x}(E) \cdot dE$. Also to note is the EEDF $f_{e-x}(E)$ which is normalized, i.e. $\int_0^\infty f_{e-x}(E) \cdot dE = 1$. In this paper, we are principally interested in extracting information on the EEDF by recording argon spectral line emissions [44]. We use the $2p_1 \rightarrow 1s_2$ transition at 750.39 nm since it is generally dominated by ground state excitation and has a minimal radiation-trapping correction. Only those electrons within the range 13–25 eV are relevant for exciting the ground state atoms into the $2p_1$ level, whereas excitation out of the $1s_5$ levels entails electrons of energy as low as 2 eV all the way through to 15 eV. Excitation from the $1s_5$ levels constitutes a significant or even a major portion of the observed radiation. Because the various $2p_1$ levels are populated by excitation out of the ground, metastable, and resonance levels with different weighting, it is possible to extract the relative ratio of low- to high-energy electrons in the plasma by examining the emissions from a number of $2p_9 \rightarrow 1s_5$ and $2p_1 \rightarrow 1s_2$ emission lines.

It is important to point out that dissociative recombination with molecular ions rapidly removes low-energy electrons, such that the low-energy portion of the electron energy distribution is depressed when oxygen or/and nitrogen is mixed with argon. The ratio Ar811/Ar750 is lower in the mixtures than in pure argon. Apart from the pure argon gas flow through the plasma jet, the amount of oxygen and nitrogen in the plume will increase with increasing distance from the jet nozzle. Therefore, away from the nozzle the mixing gas ratios between argon and oxygen/nitrogen are changing and impacting the EEDF. The dot-dashed line of Fig. 8 indicates the condition where argon is the predominant species.

Changes in the number of low-energy electrons has a greater impact on the Ar811 spectral emission away from the nozzle. The same effect has almost no impact on Ar750 spectral emission as a function of the gas flow rate. The EEDF changes by a factor of about 3 with distance. Namely, the ratio Ar811/Ar750 is largest in pure argon but falls by a factor of three when mixed with N_2–O_2. Similarly, the low-energy portion of the electron energy distribution affects the nitrogen metastable $C^3\Pi_u^+$ more than the ion N_2^+ $B^2\Sigma_u^+$, and therefore the ratio N_2(337.1 nm)/N_2^+(391.4 nm) again falls with increasing nitrogen.

4. Conclusion

Wavelength-resolved optical emission profiles suggest that the emission of argon's spectral lines show that free electrons have an important influence, together with the argon metastable atoms, on the overall spectral emission. One approach to gaining an insight into the argon metastable density is to record spectral emission from "all" lines for which the lower energy level is the metastable.

Furthermore, the experimental data indicates that air impurities like nitrogen and oxygen are less important for the creation and sustainability of plasma discharges with increasing argon flow rates. With increasing distance, nitrogen and oxygen have stronger spectral radiation than argon due to lower energy excitation levels. By increasing the argon flow rates, nitrogen and oxygen radicals start to be less present in the discharge.

The shift in the EEDF is more dependent on the distance from the nozzle than on the gas flow rate.

Spectral radiation of oxygen 777 and 845 triplets are slightly different due to the impact of molecular dissociation. O777 and O845 cannot be created by a dissociative recombination with the ground state O_2^+ because the rate is strongly peaked toward low-energy electrons.

Acknowledgements

The research leading to these results has received funding from the European Union's Seventh Framework Programme managed by REA Research Executive Agency (FP7/2007-2013) under Grant Agreement number 605125. V. Milosavljević is grateful to the Ministry of Education and Science of the Republic of Serbia under Grant No. OI171006.

References

[1] J. Meichsner, M. Schmidt, R. Schneider, and H. E. Wahner (eds.), *Nonthermal Plasma Chemistry and Physics, Plasma Surface Chemistry* (CRC Press, Boca Raton, 2013), pp. 312–387.

[2] Q. Son et al., Nonthermal Atmospheric Plasma Treatment for Deactivation of Oral Bacteria and Improvement of Dental Restoration. In *Plasma for Bio-Decontamination, Medicine and Food Security, NATO Science*, ed. Z. Machala et al. (Springer, Dordrecht, 2012), pp. 215–230.

[3] M. Schmidt, Surface Treatment. In *Non-Equilibrium Air Plasmas at Atmospheric Pressure*, ed. K. H. Becker, U. Kogelschatz, K. H. Schoenbach, and R. J. Barker (IOP Publication, Bristol, 2006), pp. 597–621.

[4] A. Fridman, *Plasma Chemistry* (Cambridge University Press, New York, 2008).

[5] M. Bonitz, J. Lopez, K. Becker, H. Thomsen (eds.), *Complex Plasmas: Scientific Challenges and Technological Opportunities* (Springer, New York, 2014).

[6] M. K. Mishra, A. K. Misra, A. Phukan, P. K. Devi, H. K. Sarma, and T. Das, Prog. Theor. Exp. Phys. **2014**, 033J01 (2014).

[7] J. Ehlbeck, U. Schnabel, M. Polak, J. Winter, T. von Woedtke, R. Brandenburg, T. von dem Hagen, and K. D. Weltmann, J. Phys. D: Appl. Phys. **44**, 013002 (2011).

[8] K.-D. Weltmann et al., Contrib. Plasma **49**, 631 (2009).

[9] S. Bornholdt, M. Wolter, and H. Kersten, Eur. Phys. J. D **60**, 653 (2010).

[10] V. Milosavljević, M. Donegan, P. J. Cullen, and D. P. Dowling, J. Phys. Soc. Japan **83**, 014501 (2014).

[11] A. Kramida et al., *NIST Atomic Spectra Database* (ver. 5.2). (National Institute of Standards and Technology, Gaithersburg, MD, 2015). (Available at: http://physics.nist.gov/asd, date last accessed April 28, 2015).

[12] R. C. Pankhurst, Proc. Phys. Soc. **52**, 388 (1940).

[13] M. P. F. Bristow and M. McChesney, Proc. Phys. Soc. **85**, 1237 (1965).

[14] G. Herzberg, *Molecular Spectra and Molecular Structure* (Van Nostrand, New York, 1963), vol. 1.

[15] E. Gudimenko, V. Milosavljević, and S. Daniels, Opt. Express **20**, 12699 (2012).

[16] R. D. Cowan, *The Theory of Atomic Structure and Spectra* (University of California Press, Berkeley, CA, 1981), Chap. 1.9.

[17] V. Milosavljević and G. Poparić, Phys. Rev. E **63**, 036404 (2001).

[18] V. Milosavljević, A. R. Ellingboe, and S. Daniels, Eur. Phys. J. D **64**, 437 (2011).

[19] D. M. Filipović, B. P. Marinković, V. Pejčev, and L. Vušković, J. Phys. B: At. Mol. Opt. Phys. **33**, 677 (2000).

[20] V. Milosavljević, N. MacGearailt, P. J. Cullen, S. Daniels, and M. M. Turner, J. Appl. Phys. **113**, 163302 (2013).

[21] C. Heslin, D. Boehm, V. Milosavljević, M. Laycock, P. J. Cullen, and P. Bourke, Plasma Medicine **4**, 153 (2014).

[22] Q. Xiong, A. Y. Nikiforov, X. P. Lu, and C. Leys, J. Phys. D: Appl. Phys. **43**, 415201 (2010).

[23] N. Sadeghi, D. W. Setser, A. Francis, U. Czarnetzki, and H. F. Dobele, J. Chem. Phys. **115**, 3144 (2001).

[24] S. V. Pancheshnyi, S. M. Starikovskaia, and A. Y. Starikovskii, Chem. Phys. **262**, 349 (2000).

[25] G.-B. Zhao, M. D. Argyle, and M. Radosz, J. Appl. Phys. **101**, 033303 (2007).

[26] J. H. Kolts and D. W. Setser, J. Chem. Phys. **68**, 4848 (1978).
[27] P. Moutard, P. Laporte, J.-L. Subtil, N. Damany, and H. Damany, J. Chem. Phys. **87**, 4576 (1987).
[28] E. A. D. Carbone, S. Hübner, J. J. A. M. van der Mullen, G. M. W. Kroesen, and N. Sadeghi, J. Phys. D: Appl. Phys. **46**, 415202 (2013).
[29] O. Zatsarinny and K. Bartschat, J. Phys. B: At. Mol. Opt. Phys. **37**, 4693 (2004).
[30] R. S. F. Chang and D. W. Setser, J. Chem. Phys. **69**, 3885 (1978).
[31] L. Zhu et al., Rev. Sci. Instrum. **80**, 023105 (2009).
[32] X. Zhu et al., J. Phys. D: Appl. Phys. **42**, 142003 (2009).
[33] S. Nunomura, M. Kondo, and H. Akatsuka, Plasma Sources Sci. Technol. **15**, 783 (2006).
[34] T. Yuji, Y. Suzaki, T. Yamawaki, H. Sakaue, and H. Akatsuka, Jpn. J. Appl. Phys. **46**, 795 (2007).
[35] H. Akatsuka, Progresses in Experimental Study of N_2 Plasma Diagnostics by Optical Emission Spectroscopy. In *Chemical Kinetics*, ed. V. Patel (InTech Rijeka, 2012).
[36] X.-J Huang, Y. Xin, L. Yang, Q.-H. Yuang, and Z.-U. Ning, Phys. Plasmas **15**, 113504 (2008).
[37] T. Yuji, T. Urayama, S. Fujii, N. Mungkung, and H. Akatsuka, Surf. Coat. Tech. **202**, 5289 (2008).
[38] T. Sakamoto, H. Matsuura, and H. Akatsuka, Jpn. J. Appl. Phys. **45**, 7905 (2006).
[39] T. Sakamoto, H. Matsuura, and H. Akatsuka, J. Appl. Phys. **101**, 023307 (2007).
[40] M. Donegan, V. Milosavljević, and D. P. Dowling, Plasma Chem. Plasma P. **33**, 941 (2013).
[41] K. Kuwano, A. Nezu, H. Matsuura, and H. Akatsuka, Proceedings of Sixth Asia-Pacific International Symposium on the Basic and Application of Plasma Technology (APSPT 6), Minghsin University of Science and Technology, Hsinchu, ROC, 207 (2009).
[42] Vogel and V. Ebert, Appl. Phys. B **72**, 127 (2001).
[43] K. J. Ritter and T. D. Wilkerson, J. Mol. Spec. **121**, 1 (1997).
[44] J. B. Boffard, R. O. Jung, C. C. Lin, and A. E. Wendt, Plasma Sources Sci. Technol. **19**, 065001 (2010).
[45] V. A. Godyak, R. B. Piejak, and B. M. Alexandrovich, J. Appl. Phys. **73**, 3657 (1993).
[46] S.-H. Seo, S. S. Kim, J.-I. Hong, C. S. Chang, and H.-Y. Chang, Appl. Phys. Lett. **76**, 149 (2000).
[47] J. T. Gudmundsson, Plasma Sources Sci. Technol. **10**, 76 (2001).
[48] H. Amemiya, J. Phys. Soc. Japan **66**, 1335 (1997).
[49] M. J. Druyvesteyn and F. M. Penning, Rev. Mod. Phys. **12**, 87 (1940).